Applied Catalysis B: Environmental 323 (2023) 122163

Contents lists available at ScienceDirect

Applied Catalysis B: Environmental

journal homepage: www.elsevier.com/locate/apcatb

Highly durable iron single-atom catalysts for low-temperature zinc-air batteries by electronic regulation of adjacent iron nanoclusters

Yang Chen [a,1], Ting He [a,b,1], Qiming Liu [c], Yongfeng Hu [d], Hao Gu [e], Liu Deng [a], Hongtao Liu [a], Youcai Liu [a], You-Nian Liu [a], Yi Zhang [a,f,*], Shaowei Chen [c,**], Xiaoping Ouyang [b,**]

[a] Hunan Provincial Key Laboratory of Micro & Nano Materials Interface Science, College of Chemistry and Chemical Engineering, Central South University, Changsha, Hunan 410083, China
[b] School of Materials Science and Engineering, Xiangtan University, Xiangtan, Hunan 411105, China
[c] Department of Chemistry and Biochemistry, University of California, 1156 High Street, Santa Cruz, CA 95064, United States
[d] Canadian Light Source, Inc. (CLSI), Saskatoon, Saskatchewan S7N2V3, Canada
[e] College of Mechanical and Electrical Engineering, Central South University, Changsha, Hunan 410083, China
[f] Key Laboratory of Materials Processing and Mold, Zhengzhou University, Ministry of Education, Zhengzhou, Henan 450002, China

ARTICLE INFO

Keywords:
Electronic regulation
Single atom catalyst
Oxygen reduction reaction
Stability
Low temperature zinc-air battery

ABSTRACT

Durability of carbon-supported Fe single-atom catalysts has remained a critical issue for metal-air batteries. Herein, Fe single atoms with adjacent Fe nanoclusters supported on nitrogen-doped carbon aerogels (NCA/Fe_{SA+NC}) are prepared via a facile two-step pyrolysis procedure using biomass hydrogels as the precursor and template. The Fe atomic centers are found to exhibit an increased 3d electron density and decreased magnetic moment by the nanoclusters. This markedly enhances the oxygen reduction reaction activity and anti-oxidation stability of the FeN_4 sites, as compared to the nanocluster-free counterparts. With NCA/Fe_{SA+NC} as the cathode catalysts, a flexible zinc-air battery delivers a remarkable performance even at −40 °C, with an open circuit voltage as high as 1.47 V, power density 49 mW cm^{-2}, and excellent durability after 2300 continuous recharging/charging cycles. The performance is even higher at ambient temperature. These results highlight the significance of electronic manipulation in enhancing the durability of single atom catalysts.

1. Introduction

Electrocatalysis of oxygen reduction reaction (ORR) is a cornerstone of a range of electrochemical energy technologies, such as fuel cells and metal-air batteries [1–4]. Whereas platinum-based composites have been the benchmark catalysts for ORR, development of nonprecious metal catalysts has become imperative for cost and sustainability reasons [5,6]. In fact, transition metal−nitrogen−carbon (M−N−C) composites have been recognized as viable alternatives thanks to their high activity and low costs [7–10]. Among these, single (metal) atom catalysts (SACs) have been attracting extensive attention, where manipulation of the configurations of the atomically dispersed metal sites can be exploited for the optimization of the electrocatalytic activity [11–16]. In particular, Fe SACs, with FeN_x moieties embedded within porous carbon, have been found to exhibit a high ORR activity, where the half-wave potential ($E_{1/2}$) is comparable to that of commercial Pt/C in both acidic and alkaline media [17,18]. Yet, carbon-based SACs are known to exhibit apparent degradation during prolonged electrode reactions, due to demetallation, carbon oxidation and bulk carbon corrosion, leading to poor stability [19,20], which has become a major obstacle in practical applications.

To mitigate such issues, research has primarily focused on two strategies, increased graphitization of the carbon scaffold and stabilization of the metal active sites. For example, carbon corrosion can be alleviated by integrating metal sites into highly graphitic graphene or carbon nanotubes [21,22]. Additionally, a second metal element can be incorporated into SACs to impede the undesired Fenton reactions [23,24]. Nevertheless, whereas these strategies indeed yield improved

* Corresponding author at: Hunan Provincial Key Laboratory of Micro & Nano Materials Interface Science, College of Chemistry and Chemical Engineering, Central South University, Changsha, Hunan 410083, China.
** Corresponding authors.
E-mail addresses: yzhangcsu@csu.edu.cn (Y. Zhang), shaowei@ucsc.edu (S. Chen), oyxp2003@aliyun.com (X. Ouyang).
[1] These authors contributed equally to this work.

https://doi.org/10.1016/j.apcatb.2022.122163
Received 15 July 2022; Received in revised form 28 October 2022; Accepted 9 November 2022
Available online 11 November 2022

stability, drawbacks are clear, as increasing graphitization diminishes carbon defects and compromises electrocatalytic activity, and structural engineering of the metal sites requires tedious operations. Thus, development of facile and effective strategies to enhance the stability and concurrently retain the high activity of SACs is highly desired. This is the main motivation of the present study.

Herein, we describe an effective strategy based on electronic regulation by adjacent metal nanoclusters to improve the stability of Fe SACs without compromising the ORR activity. Fe–N–C nanocomposites typically contain both durable and non-durable FeN_x sites [19]. In the former, the metal centers retain the Fe(II) valency during electrode reactions, while in the latter, the metal centers switches between the oxidation state of Fe(III) and Fe(II) and can be easily transformed into ferric oxides. This suggests that the stability of the FeN_x sites can be strengthened by impeding the oxidation of Fe(II) to Fe(III). Theoretical studies have shown that electron-rich metallic nanoparticles in the close proximity may inhibit the oxidation of the FeN_x sites via electron-transfer interactions [25]; yet, such electron transfer has to be relatively weak so as not to impair the ORR activity [26–29]. Thus, it is anticipated that the FeN_x stability can be improved by introducing adjacent small-sized metal nanoclusters, where the weak/indirect electron transfer bridged by carbon atoms helps suppress the oxidation of Fe (II) to Fe(III). Notably, metal nanoclusters may also endow the nanocomposites with bifunctional oxygen catalytic activity, with a good performance towards oxygen evolution reaction (OER) as well, an essential feature for rechargeable metal-air batteries [30].

Experimentally, Fe nanoclusters were introduced to the proximity of the FeN_x single atom sites embedded within N-doped carbon aerogels (NCA/Fe_{SA+NC}) via a facile two-step pyrolysis method using biomass hydrogels as the precursor and template [31]. First principles calculations show an increased 3d electron density and reduced magnetic moment of the Fe centers, suggesting positive effects on the ORR activity and anti-oxidation stability of the FeN_4 sites. Electrochemically, the NCA/Fe_{SA+NC} composites indeed exhibited not only an excellent ORR performance, with a half-wave potential ($E_{1/2}$) of +0.92 V versus reversible hydrogen electrode (RHE), but also remarkably enhanced stability, as compared to that without Fe nanoclusters (NCA/Fe_{SA}). With the NCA/Fe_{SA+NC} as the cathodic catalysts, the assembled flexible Zn-air battery exhibited a high power density and remarkable durability at both ambient and even sub-zero temperatures (down to −40 °C). These results offer an effective strategy in optimizing both electrocatalytic activity and stability of M−N−C composites, a critical step in advancing commercialization of electrochemical energy technologies.

2. Experimental section

2.1. Sample preparation

Details of chemicals are included in the Supporting Information. In a typical reaction, a blood-red dispersion was prepared by mixing gelatin (180.0 mg), nano-SiO_2 (90.0 mg), $FeCl_2{\cdot}4H_2O$ (23.9 mg) and 1,10-phenanthroline monohydrate (PM, 71.4 mg) into 7.5 mL of ultrapure water in a 60 ℃ water bath for 20 min. The resulting mixture was self-assembled into a hydrogel in a −4 ℃ refrigerator, which was denoted as G-Si/FePM.

The lyophilized G-Si/FePM hydrogel was then used to prepare NCA/Fe_{SA} and NCA/Fe_{SA+NC} by following two slightly different routes. For the former, G-Si/FePM was pyrolyzed at 900 ℃ at a heating rate of 5 ℃ min^{-1} under a mixed atmosphere (97% Ar + 3% H_2) for 3 h. The resulting product was then subject to chemical etching by 4% HF to remove the SiO_2 nanoparticle templates and the Fe clusters, and dried at 60 ℃ in vacuum for 1 h, affording NCA/Fe_{SA}.

To prepare NCA/Fe_{SA+NC}, the lyophilized G-Si/FePM hydrogel was pyrolyzed at 500 ℃ at a heating rate of 5 ℃ min^{-1} under an argon atmosphere for 2 h, followed by etching in 0.5 M NaOH at 80 ℃ to remove SiO_2 (denoted as NCA/Fe-500). The NCA/Fe-500 powders were then subject to a second pyrolysis at a heating rate of 5 ℃ min^{-1} to 900 °C under a mixed atmosphere (3% H_2 + 97% Ar) for 3 h to produce NCA/Fe_{SA+NC}. The gas flow rates during pyrolysis were all set at 100 mL min^{-1}.

Four additional control samples were prepared in the same manner as that for NCA/Fe_{SA+NC} except for the following variations: NCA_A/Fe_{SA+NC} and NCA_C/Fe_{SA+NC} by using agar and chitosan instead of gelatin, respectively; whereas NCA/Fe_{SA+NC}-L and NCA/Fe_{SA+NC}-H by using 60 mg and 120 mg SiO_2, respectively.

Experimental details about the synthesis of polyacrylic acid (PAA) hydrogel and polyacrylamide (PAM) organohydrogel electrolytes, electrochemical measurements (Fig. S1), as well as theoretical calculations were included in the Supporting Information.

2.2. Construction and testing of flexibility quasi-solid Zn-air battery

Quasi-solid Zn-air battery entailed a typical sandwich configuration (Fig. S2), with the air cathode and Zn plate placed on the two opposite sides of the PAA hydrogel electrolyte. The air cathode was composed of a catalyst layer, a gas diffusion layer and a Ni foam layer. The catalyst layer was prepared by thoroughly mixing the aerogel catalyst, acetylene black and polytetrafluoroethylene (PTFE) emulsion at a mass ratio of 6:1:3 in ethanol. Then, the catalyst layer, Ni foam and gas diffusion layer were compressed by a roller press to produce the air electrode, which was dried at 60 ℃ in vacuum for 3 h and cut into pieces of 1.0 cm × 1.0 cm before use. As a comparison, a reference cathode was prepared in the same manner but with commercial Pt/C-RuO_2. A low-temperature Zn-air battery was assembled in the same manner except that the PAA hydrogel electrolyte was replaced by the PAM oranohydrogel electrolyte.

The active material films on the electrode surfaces for various electrochemical measurements ranged from 0.05 to 0.2 mm in thickness, with a mass loading up to 15 mg cm^{-2}, as listed in Table S1. More details about the tests of the battery performance can be found in the Supporting Information.

3. Results and discussion

3.1. Synthesis and structural characterization

In the synthesis of NCA/Fe_{SA+NC} nanocomposites (Fig. 1a), a gelatin hydrogel containing Fe-phenanthroline (Fe-PM) complex and nano-SiO_2 was firstly prepared by a freeze-thawing method at −4 and 20 ℃. The obtained freeze-dried hydrogel showed a 3D honeycomb-like structure (Fig. S3), which was then transformed into a N-doped carbon aerogel decorated with atomically dispersed Fe sites by pyrolysis at 500 ℃ followed by removal of the SiO_2 templates by NaOH etching. A second pyrolysis was carried out at 900 ℃, where part of the Fe atoms that were weakly bound to the carbon skeletons were aggregated into nanoclusters near the Fe single atoms, producing NCA/Fe_{SA+NC}. For comparison, direct pyrolysis of the hydrogel precursor at 900 ℃ and etching by HF yielded N-doped carbon aerogels with dispersion of Fe single atoms only (NCA/Fe_{SA}).

The morphological and structural details of the obtained carbon aerogels were first probed by scanning electron microscopy (SEM) and transmission electron microscopy (TEM) measurements. Fig. S4 shows two representative SEM images, where the carbon aerogels can be seen to retain the 3D structures with abundant pores that might help impede the excessive aggregation of metal atoms into large nanoparticles. This is indeed manifested in the TEM images in Fig. 1b, where no large metal nanoparticle (over 10 nm in diameter) can be observed in the NCA/Fe_{SA+NC} sample. In high-angle annular dark field-scanning transmission electron microscopy (HAADF-STEM) measurements, the NCA/Fe_{SA+NC} composites can be found to consist of both metal nanoclusters (under 10 nm in diameter) and single atoms (red cycles) (Fig. 1c), where the nanoclusters exhibited clearly-defined lattice fringes, with the

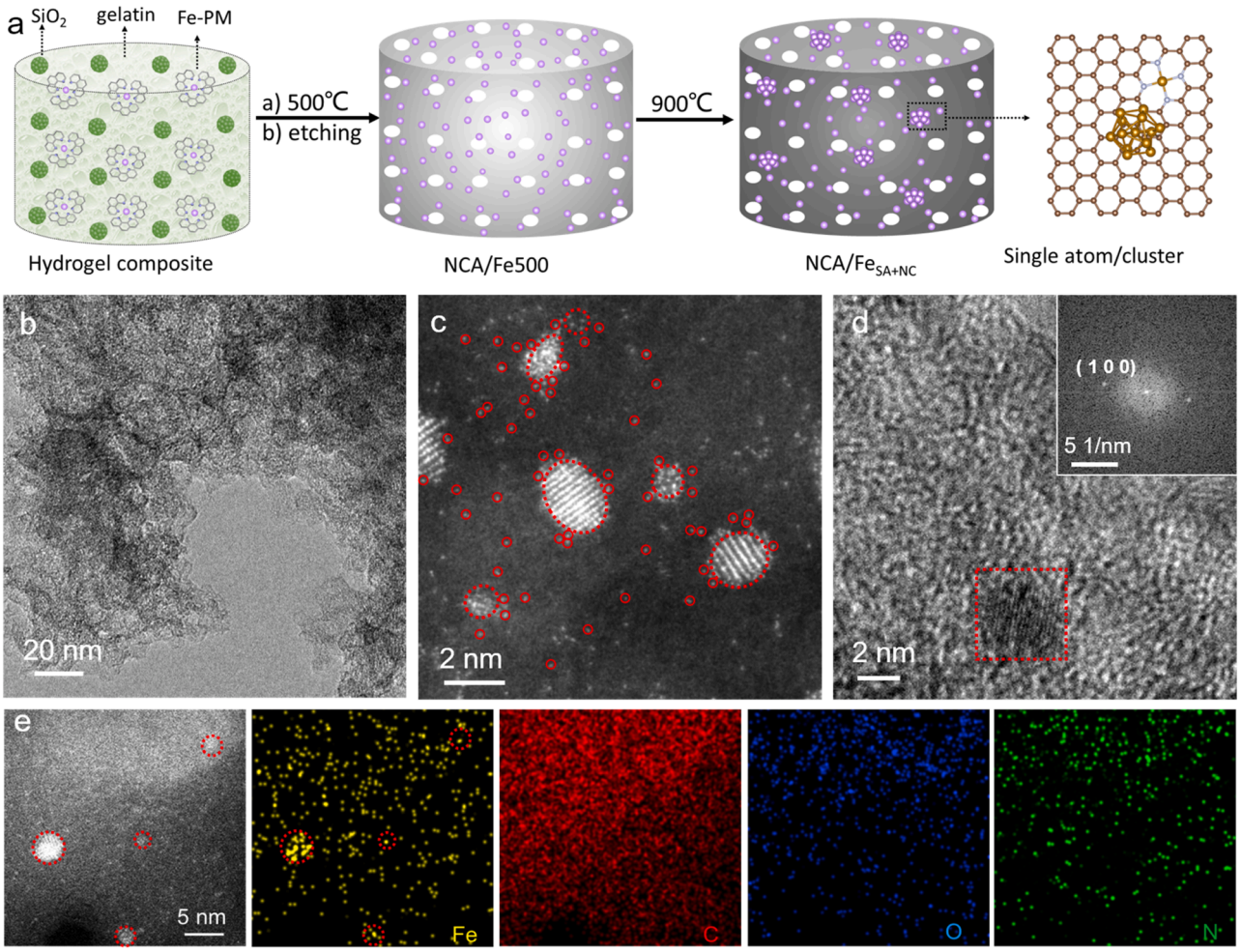

Fig. 1. (a) Schematic illustration of the preparation of NCA/Fe_{SA+NC}. (b) TEM and (c) HAADF-STEM images of NCA/Fe_{SA+NC}. (d) HRTEM image of a typical metal cluster in NCA/Fe_{SA+NC}. Inset is the Fourier transform of the red region in (d). (e) HAADF-STEM image and elemental maps of NCA/Fe_{SA+NC}.

interplanar distances of 2.13 Å and 1.84 Å respectively arising from the (100) and (101) planes of metallic Fe (PDF#34–0529) (Fig. 1d and inset, Fig. S5a). The formation of both metallic Fe nanoclusters and single atoms in the carbon aerogel is also confirmed in elemental mapping analysis based on energy-dispersive X-ray spectroscopy (Fig. 1e). For comparison, for NCA/Fe_{SA} that was prepared by one-step pyrolysis, only single Fe atoms were resolved (Fig. S5b-c).

In N_2 adsorption-desorption measurements, both the NCA/Fe_{SA+NC} and NCA/Fe_{SA} composites exhibited a Type IV isotherm [32], indicating the formation of a complex porous network dominated by mesopores ranging from 5 to 15 nm (Fig. S6 and inset). The specific surface area was estimated to be 899 $m^2\ g^{-1}$ of NCA/Fe_{SA}, and decreased to 574 $m^2\ g^{-1}$ for NCA/Fe_{SA+NC}, likely because part of the nanopores in NCA/Fe_{SA} were blocked by the metal nanoclusters. In X-ray diffraction (XRD) measurements (Fig. S7a), both NCA/Fe_{SA+NC} and NCA/Fe_{SA} can be observed to exhibit a broad diffraction peak at $2\theta \approx 25°$, arising from the (002) diffraction of graphitic carbon (PDF#65–6212), suggesting effective graphitization of the hydrogel precursors into aerogels [33]. Two additional diffraction peaks can be resolved at 42.5° and 50.1° for NCA/Fe_{SA+NC} but absent in NCA/Fe_{SA}, which can be ascribed to the (100) and (101) facets of hexagonal Fe (PDF#34–0529), in excellent agreement with the lattice spacings (2.13 and 1.84 Å) observed in the above HRTEM measurements (Fig. 1c, S5a and inset). In Raman spectroscopic measurements (Fig. S7b), both NCA/Fe_{SA+NC} and NCA/Fe_{SA} exhibited a D band at 1348 and a G band at 1590 cm^{-1} [34], with a slightly lower peak intensity ratio for the former ($I_D/I_G = 0.89$) than for the latter (0.92), suggesting a somewhat higher degree of graphitization. This is consistent with the sharper carbon (002) diffraction peak of NCA/Fe_{SA+NC} (Fig. S7a), and can facilitate electron transfer and electrocatalytic reactions (vide infra) [35,36].

X-ray photoelectron spectroscopy (XPS) measurements were then conducted to examine the elemental composition and valence state of the carbon aerogels. From the survey spectra in Fig. S8, the elements of C 1s, N 1s, O 1s and Fe 2p electrons can be clearly resolved at about 284, 400, 530, and 710 eV in both NCA/Fe_{SA+NC} and NCA/Fe_{SA} carbon aerogels, with a Fe content of 1.8 and 1.0 wt%, respectively. Consistent results were obtained from inductively coupled plasma-optical emission spectroscopy (ICP-OES) measurements (Table S2). Fig. 2a shows the high-resolution scans of the Fe 2p electrons. One can see that NCA/Fe_{SA+NC} contains three doublets, 708.0/721.2 eV (blue peaks) for Fe(0), 709.8/723.2 eV (magenta peaks) for Fe(II) and 713.9/727.3 eV (orange peaks) for Fe(III); by contrast, only the Fe(II) and Fe(III) species can be resolved in NCA/Fe_{SA}. This is consistent with the formation of both Fe nanoclusters and single atoms in the former, whereas only Fe single atoms in the latter. Notably, the Fe(II) and Fe(III) binding energies of NCA/Fe_{SA+NC} were about 0.2 eV lower than those of NCA/Fe_{SA} (Table S3), suggesting electron-enriched Fe centers in the former likely due to electron-donation from the nearby Fe nanocluster, which may facilitate ORR electrocatalysis (vide infra). In addition, the atomic ratio of Fe(II) to Fe(III) was markedly higher in NCA/Fe_{SA+NC} (1.5) than in NCA/Fe_{SA} (1.1), suggesting enhanced anti-oxidation stability of the former [19]. In the O 1 s spectra (Fig. S9), the C═O and C−O/O−H peaks can be resolved at ca. 531.8 and 532.0 eV, respectively, but no metal−O (M−O) peak under 530 eV for both aerogel composites.

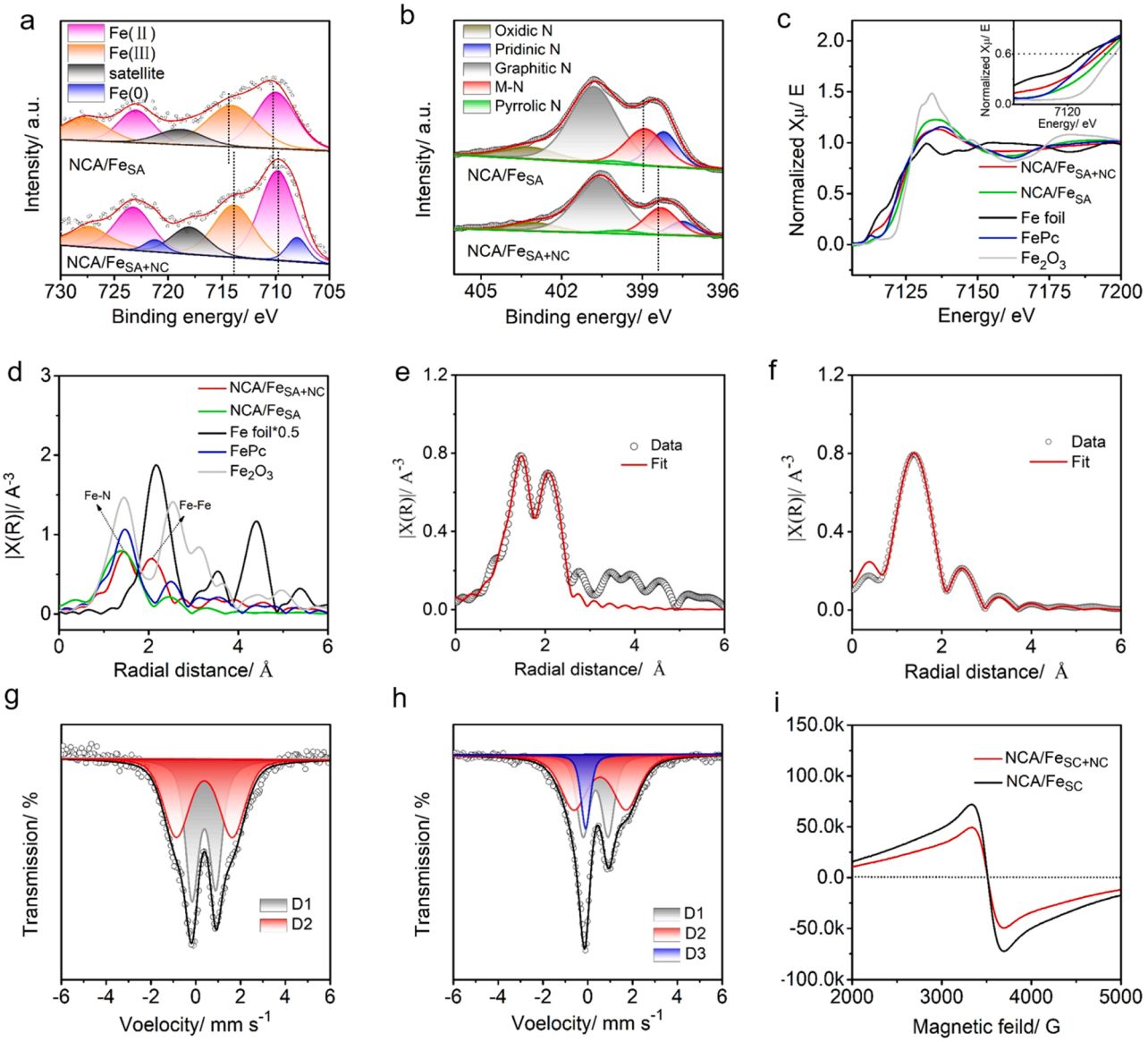

Fig. 2. High-resolution XPS scans of the (a) Fe 2p and (b) N 1s electrons of NCA/Fe$_{SA+NC}$ and NCA/Fe$_{SA}$. (c) Normalized Fe K-edge XANES spectra and (d) Fourier transform k^3-weighted Fe K-edge EXAFS spectra of NCA/Fe$_{SA+NC}$, NCA/Fe$_{SA}$, Fe foils, FePc and Fe$_2$O$_3$. Inset to panel (c) is the zoom in of the absorption edge. EXAFS fittings of (e) NCA/Fe$_{SA+NC}$ and (f) NCA/Fe$_{SA}$. ^{57}Fe Mössbauer spectra of (g) NCA/Fe$_{SA}$ and (h) NCA/Fe$_{SA+NC}$. (i) EPR spectra of NCA/Fe$_{SA+NC}$ and NCA/Fe$_{SA}$.

Deconvolution of the corresponding N 1 s spectra yielded 5 species, pyridinic (398 eV), metal−N (M−N) (399 eV), pyrrolic (400 eV), graphitic (401 eV), and oxidic N (403 eV) (Fig. 2b and Table S4) [37–40], suggesting that the Fe single atoms in the carbon aerogels were most likely chelated to the N dopants forming FeN$_x$ moieties. Of note is that the Fe−N species in NCA/Fe$_{SA+NC}$ show a decrease of the binding energy by 0.4 eV as compared to that in NCA/Fe$_{SA}$, again, consistent with the electron-enriched Fe centers in the former likely due to electron transfer from the adjacent Fe nanoclusters.

The coordination configuration of the FeN$_x$ moieties was then probed by X-ray absorption spectroscopy (XAS) measurements. Fig. 2c depicts the Fe K-edge X-ray absorption near-edge structure (XANES) profiles of the series of samples, where the white-line intensity can be seen to vary in the order of Fe foil < NCA/Fe$_{SA+NC}$ ≈ iron(II) phthalocyanine (FePc) < NCA/Fe$_{SA}$< Fe$_2$O$_3$, consistent with the formation of both Fe nanoclusters and Fe single atoms in NCA/Fe$_{SA+NC}$ but only Fe single atoms in NCA/Fe$_{SA}$. This variation can also be found in the absorption edge energy (Fig. 2c inset). Fig. 2d displays the corresponding Fourier transforms of the extended X-ray absorption fine structure (EXAFS) profiles. FePc, NCA/Fe$_{SA+NC}$ and NCA/Fe$_{SA}$ all exhibited a primary peak for Fe−N bonds at ca. 1.4 Å (no Fe−O bonds were formed, as suggested by the above XPS measurements); and for NCA/Fe$_{SA+NC}$ a second peak appeared at ca. 2.2 Å, likely due to the Fe−Fe bonds, in accord with the formation of Fe nanoclusters in the sample — this peak was clearly defined with Fe foils. The coordination numbers (CN) and bond lengths of Fe−N and Fe−Fe were then estimated by fitting the EXAFS spectra (Fig. 2e-f and S10). As listed in Table S5, the Fe−Fe path of NCA/Fe$_{SA+NC}$ can be seen to exhibit a bond length of 2.50 Å, consistent with that of Fe foil, but the CN is markedly lower (2 vs. 8), due to the formation of small-sized metal clusters [41]. For the Fe−N path, NCA/Fe$_{SA+NC}$ showed a CN of 3.6 and a bond length of 1.91 Å, slightly smaller than that of NCA/Fe$_{SA}$ (4.2 and 1.99 Å), likely due to electron transfer to the FeN$_4$ sites from Fe clusters in the close proximity. Collectively, these results confirm that NCA/Fe$_{SA+NC}$ is composed mostly of FeN$_4$ moieties and adjacent Fe clusters, whereas only FeN$_4$ in NCA/Fe$_{SA}$.

Consistent results were obtained in ^{57}Fe Mössbauer spectroscopy measurements [42]. Generally, carbon composites containing FeN$_x$C$_y$ moieties exhibit at least two distinct doublets, D1 and D2 that are

empirically ascribed to high-spin Fe(III) and medium/low-spin Fe(II), respectively, with a similar isomer shift (δ) of 0.30 − 0.45 mm s^{-1} and quadrupole splitting energy (ΔE_{QS}) of about 1.0 and 2.5 mm s^{-1}, respectively [43]. As shown in Fig. 2g-h, both D1 and D2 can be resolved in NCA/Fe_{SA+NC} and NCA/Fe_{SA}, with an additional peak (D3, $\delta = -0.06$ mm s^{-1}) for NCA/Fe_{SA+NC} due to Fe nanoclusters. Table S6 lists the percentage of D1 and D2 in the two carbon aerogels. One can see that D2 accounts for 50.7% in NCA/Fe_{SA}, and is markedly higher at 58.1% for NCA/Fe_{SA+NC}, suggesting effective chemical interaction between Fe single atoms and nanoclusters in the latter, in accord with results from the above XPS measurements. It should be noted that the D2 moieties exhibit better ORR stability than D1 [19], thus the higher fraction of D2 in NCA/Fe_{SA+NC} is anticipated to lead to enhanced stability as compared to NCA/Fe_{SA} (vide infra).

In electron paramagnetic resonance (EPR) measurements (Fig. 2i), both NCA/Fe_{SA+NC} and NCA/Fe_{SA} exhibited a clear signal centered at ca. 3500 G within the magnetic field strength of 2000–5000 G, and the peak-to-peak amplitude was clearly weaker for the former than for the latter. This further confirms a decreased spin state of FeN_4 by the neighboring Fe nanoclusters in NCA/Fe_{SA+NC} [44].

3.2. Theoretical computation

The interaction between Fe single atom sites and adjacent Fe nanoclusters was then examined by theoretical calculations (computational details are included in the Supporting Information), involving four configurations, FeN_4 alone (S0 site) and FeN_4-Fe_{13} cluster pairs at a distance of 3 Å (S1 site), 5 Å (S2 site) and 8 Å (S3 site) on graphitic carbon (Fig. 3a). From the ORR free energy diagrams (+0.90 V) (Fig. 3b and S11-S14), it can be seen that the first and second electron-transfer steps on S0, S1, S2, and S3 are all exothermic, while the third and fourth electron-transfer steps are endothermic, and the final step, the desorption of −OH, is the rating determining step (RDS) [45]. The desorption energy of −OH (ΔG_{OH^*}) is 0.36 eV on the S0 site, and slightly lower at 0.33 eV on S1, 0.30 eV on S2, 0.34 on S3. This suggests that the ORR electrocatalysis of the FeN_4 site can be boosted by the adjacent Fe nanoclusters. Among the series, the S2 site shows the lowest energy barrier (0.30 V) and highest limiting potential (0.60 V), and is thus kinetically favorable for ORR (Fig. 3c).

In recent studies [19,46–48], the electron spin states of the metal active sites have been found to be closely related to the activity and/or stability of the FeN_x catalysts. Thus, density functional theory (DFT) calculations were performed to estimate the Fe magnetic moment of the FeN_4 moieties on these sites to further explore the interaction with the Fe nanoclusters (Fig. 3d), which was 1.94 μB for the S0 site and reduced to 1.75 μB for S3, 1.68 μB for S2 and 1.65 μB for S3, in good accord with results from the above ^{57}Fe Mössbauer measurements. This signifies apparent electronic regulation of the Fe single sites by the adjacent Fe

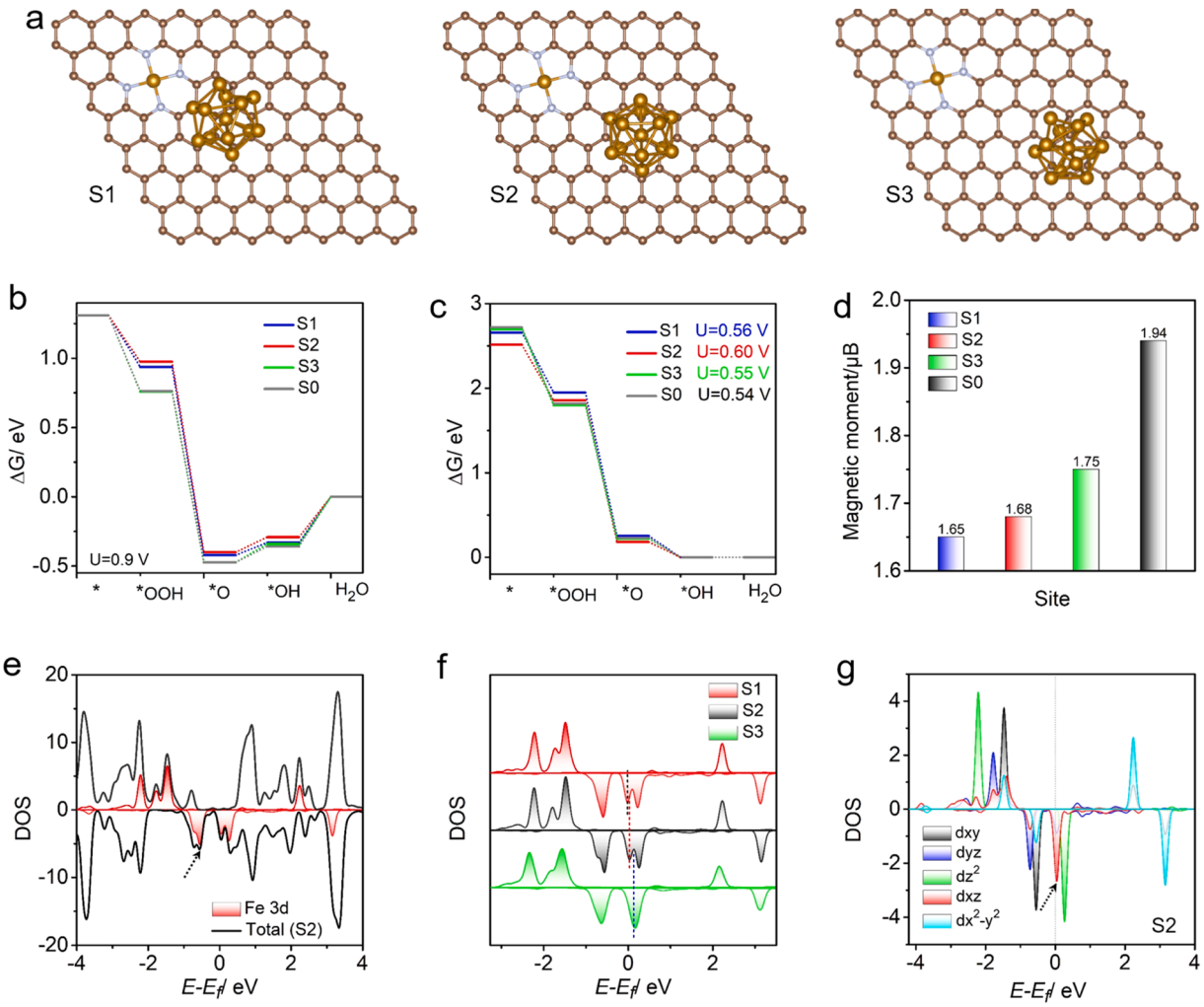

Fig. 3. (a) Optimized configurations of the S1, S2 and S3 sites, where the distance between FeN_4 and Fe nanocluster is 3 Å for S1, 5 Å for S2, and 8 Å for S3. Free energy diagrams of the S1, S2, S3 and S0 sites (b) at 0.90 V vs. RHE and (c) at their respective limiting potentials. (d) Magnetic moments of the S1, S2, S3 and S0 sites. (e) DOS of the S2 site and its Fe 3d orbitals in FeN_4. (f) DOS of Fe 3d electrons in the S1, S2 and S3 sites. (g) DOS of the five Fe 3d orbitals at the S2 site.

nanoclusters, which became strengthened with a decreasing distance between them. Further insights into the electronic regulation effect can be obtained from the analysis of the density of states (DOS). From Fig. 3e, one can see that the Fe 3d electrons make the major contributions to the S2 DOS near the Fermi level (signified by the black arrow), indicating that the Fe atoms in the FeN_4 serve as the dominant active site. Similar results can be obtained at the S1 and S3 sites (Fig. S15). Fig. 3f compares the DOS of the Fe 3d electrons at the S1, S2 and S3 sites. The marked states shifted negatively as the nanoclusters became increasingly close to FeN_4, suggesting that the Fe center in FeN_4 can readily accept electrons from the adjacent Fe nanoclusters, and the marked states at S2 was the closest to the Fermi level. This optimal configuration is in accord with the results from the free energy diagrams (Fig. 3b-c). The electron transfer interaction is also confirmed by analysis of the Bader charge of these sites, which varies in the order of S1 > S2 > S3 > S0 (Table S7).

Fig. 3g and S16 show the DOS of the five Fe 3d orbitals at the S1, S2 and S3 sites, where the marked states near Fermi level can be seen to be mainly related to the d_{xz} orbitals, in sharp contrast to the d_{xy} orbital for the S0 site (Fig. S17). As the nanocluster became closer (from S3 to S1), the increasing electron donation from the nanoclusters led to the formation of a filled d_{xy} orbital and partly filled d_{xz} orbital in FeN_4. This suggests a distinct evolution of the electron configuration and hence magnetic moment from S0 to S1, S2, and S3, as a result of electron transfer from the Fe nanoclusters to single atoms. This is indeed manifested in electrochemical measurements of the ORR activity and stability, as detailed below.

3.3. ORR activity and durability

The ORR activity of the aerogel composites was then evaluated in 0.1 M KOH, with commercial Pt/C as a comparative benchmark. The ORR polarization curves were acquired with a rotating disk electrode (RDE) at 1600 rpm (Fig. 4a and S18), where NCA/Fe_{SA+NC} can be seen to outperform others in the sample series. From Fig. 4b, one can see that NCA/Fe_{SA+NC} exhibited an onset potential (E_{onset}) of +1.05 V and half-wave potential ($E_{1/2}$) of +0.92 V, as compared to +1.01 and +0.90 V for NCA/Fe_{SA} and 0.98 and +0.86 V for commercial Pt/C. Consistent results were obtained in electrochemical impedance spectroscopy (EIS) analysis, where the charge-transfer resistance (R_{ct}) of NCA/Fe_{SA+NC} (65.9 Ω) was markedly lower than that of NCA/Fe_{SA} (89.9 Ω) (Fig. S19). In fact, the ORR activity of NCA/Fe_{SA+NC} is among the best of relevant Fe-N-C composite catalysts [49]. In addition, the kinetic current density (J_k) at +0.85 V was estimated by Koutecky-Levich analysis (Fig. 4b and S20), which was 18.7 mA cm^{-2} for NCA/Fe_{SA+NC}, about 2 times higher than those of NCA/Fe_{SA} (10.8 mA cm^{-2}) and Pt/C (9.5 mA cm^{-2}). The corresponding Tafel slope was ca. 60 mV dec^{-1} for NCA/Fe_{SA+NC}, 58 mV dec^{-1} for NCA/Fe_{SA}, and much higher for Pt/C (75 mV dec^{-1}) (Fig. 4c), indicating a fast reaction kinetic process. The repeatability of NCA/Fe_{SA+NC} was also examined by RDE measurements with three parallel batches of samples (Fig. S21), where the standard deviation of $E_{½}$ and Tafel slopes was merely 0.16% and 2.4%, respectively.

Results from the rotating ring disk electrode (RRDE) measurements indicate that ORR followed the efficient $4e^-$ pathway on NCA/Fe_{SA+NC} and NCA/Fe_{SA}, similar to Pt/C, and NCA/Fe_{SA+NC} exhibited the lowest average H_2O_2 yield (2.65%) and highest average electron transfer number (n = 3.96) in the potential range of +0.2 to +0.9 V (Fig. S22) [50]. This remarkable performance of NCA/Fe_{SA+NC} is most likely due to electronic regulation of the Fe single atom sites by the adjacent Fe nanoclusters.

Acid etching was then performed to differentiate the contributions of Fe clusters and single atoms in NCA/Fe_{SA+NC} to ORR electrocatalysis.

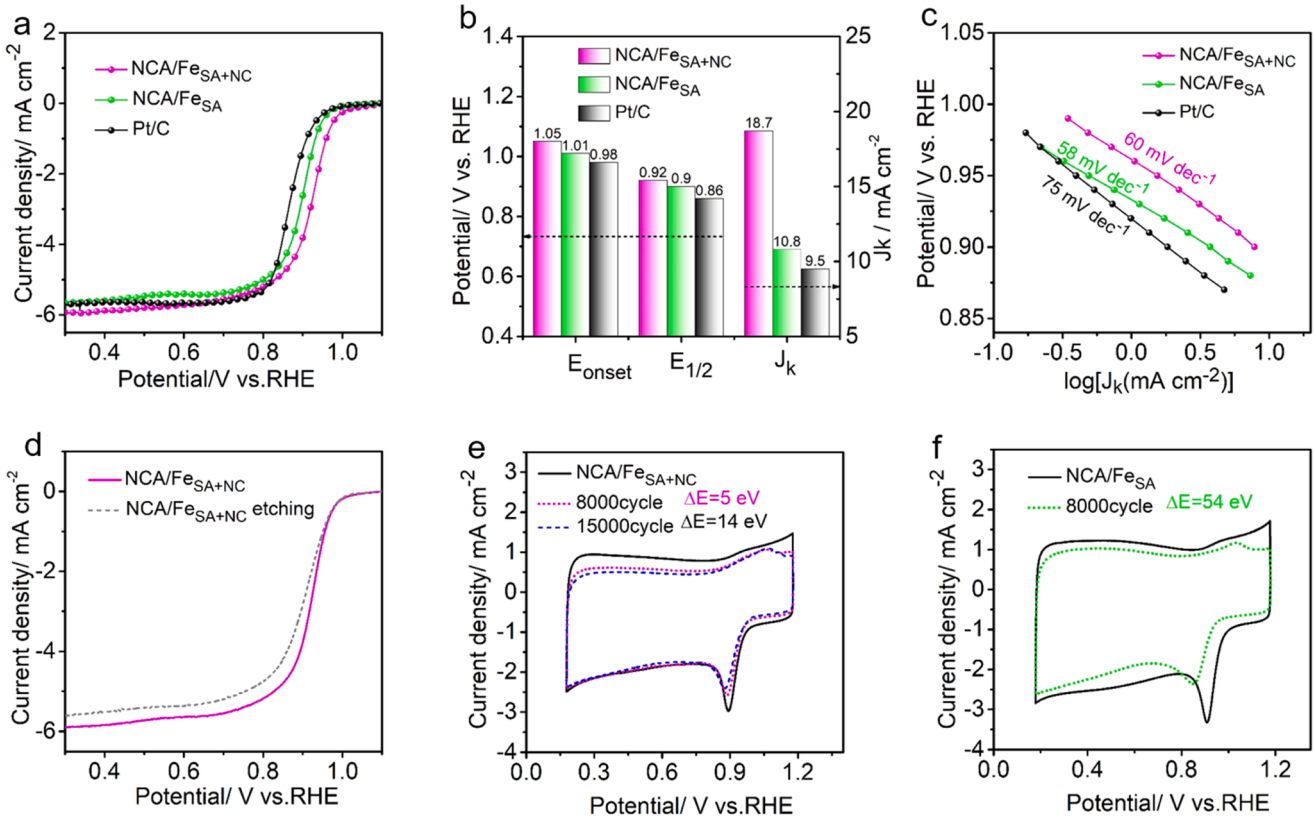

Fig. 4. (a) ORR polarization curves at the rotation rate of 1600 rpm in oxygen-saturated 0.1 M KOH. (b) Comparison of E_{onset}, $E_{1/2}$ and J_k and (c) the corresponding Tafel slopes for NCA/Fe_{SA+NC}, NCA/Fe_{SA} and commercial Pt/C. (d) ORR polarization curves of NCA/Fe_{SA+NC} before and after acid etching. Durability tests of (e) NCA/Fe_{SA+NC} and (f) NCA/Fe_{SA}.

After etching in 0.5 M H_2SO_4, the Fe clusters vanished and concurrently distinct micropores appeared, as attested in TEM measurements (Fig. S23). The removal of Fe clusters resulted in a negative shift of $E_{1/2}$ by ca. 20 mV to +0.90 V, which was identical to that of NCA/Fe_{SA} (Fig. 4d). This suggests that the ORR activity was primarily due to the Fe single atoms and further enhanced by electronic interactions with Fe nanoclusters. In addition, the electrocatalytic stability of NCA/Fe_{SA+NC} and NCA/Fe_{SA} was evaluated and compared by cyclic voltammetry (CV) measurements. After 8,000 continuous cycles within the potential range of + 0.2 to + 1.2 V, the former displayed a negative potential shift of the ORR peak by only 5 mV (Fig. 4e), less than one tenth of that for the latter (54 mV, Fig. 4f). This confirmed that the clearly enhanced stability of NCA/Fe_{SA+NC} was due to the electronic regulation of the Fe nanoclusters (in fact, the peak potential shifted negatively by only 14 mV after 15,000 continuous cycles, Fig. 4e).

XPS measurements were also carried out to compare the aerogel structures after the long-term cycle tests (Fig. 5). From the Fe 2p spectra before and after 8,000 CV cycles, one can see that NCA/Fe_{SA} exhibited a positive shift of the binding energy of the main peak by 0.9 eV (Fig. 5a), whereas only 0.1 eV for NCA/Fe_{SA+NC} (Fig. 5b), indicating drastically enhanced anti-oxidation of the Fe species in the latter (as the presence of other additives such as Nafion and carbon black made it difficult to deconvolute the peaks, the peaks were used directly for comparison). Consistent results were obtained in the O 1s, N 1s and C 1s spectra (Fig. S24, Table S8-S10).

As mentioned previously, the decay of the ORR performance of FeN_x composites is largely due to the oxidation of the Fe sites and aggregation into metal oxide nanoparticles. TEM measurements were therefore conducted to examine and compare the morphological evolution of NCA/Fe_{SA} and NCA/Fe_{SA+NC} after the stability tests. From Fig. 5c-d, one can see that whereas monoclinic Fe_2O_3 nanocrystals can be identified in both NCA/Fe_{SA} and NCA/Fe_{SA+NC}, as attested in selected area electron diffraction (insets to Fig. 5c-d), the number of such nanoparticles is significantly lower in NCA/Fe_{SA+NC} than in NCA/Fe_{SA}. This further confirms enhanced anti-oxidation (demetalization) of NCA/Fe_{SA+NC}, consistent with the XPS results.

3.4. Zn-air battery performance

Previous studies have shown that both FeN_4 sites and Fe nanoclusters may be active towards oxygen evolution reaction (OER) [51,52]. Therefore, the OER activity of these carbon aerogels and their application as bifunctional cathode catalysts for rechargeable metal-air batteries was also assessed. Fig. 6a shows the OER polarization profiles of the carbon aerogels in 1.0 M KOH with 90% iR correction. NCA/Fe_{SA+NC} exhibits not only a lower potential to reach the current density of 10 mA cm^{-2} ($E_{OER,10}$ = +1.57 V), but also a lower Tafel slope (71.5 mV dec^{-1}), as compared to NCA/Fe_{SA} (+1.61 V and 97.1 mV dec^{-1}) (Fig. S25). This suggests significant potential of NCA/Fe_{SA+NC} for OER electrocatalysis as well, and acid leaching experiments showed that the activity also arose mostly from Fe single atoms and could be enhanced with Fe nanoclusters (Fig. S26). In fact, the potential gap, $\Delta E = E_{OER,10} - E_{1/2}$, is only 0.65 V for NCA/Fe_{SA+NC}, 60 mV lower than that of NCA/Fe_{SA} (0.71 V), and superior to most bifunctional oxygen electrocatalysts reported recently (Fig. 6a inset) [53–58].

To explore the practical application of the carbon aerogels in

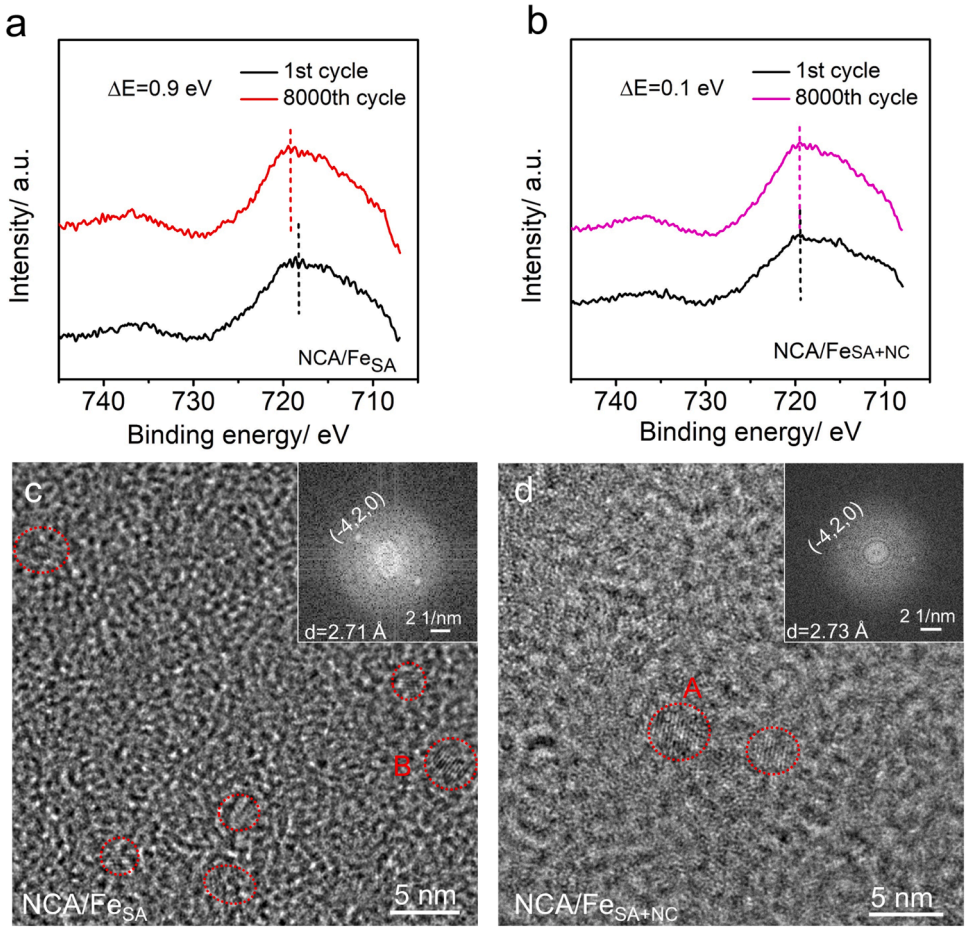

Fig. 5. Fe 2p XPS spectra of (a) NCA/Fe_{SA} and (b) NCA/Fe_{SA+NC} before and after durability tests. HRTEM images of (c) NCA/Fe_{SA} and (d) NCA/Fe_{SA+NC} after durability tests. Insets are the selected area electron diffraction patterns of areas B and A in panel (c) and (d), respectively.

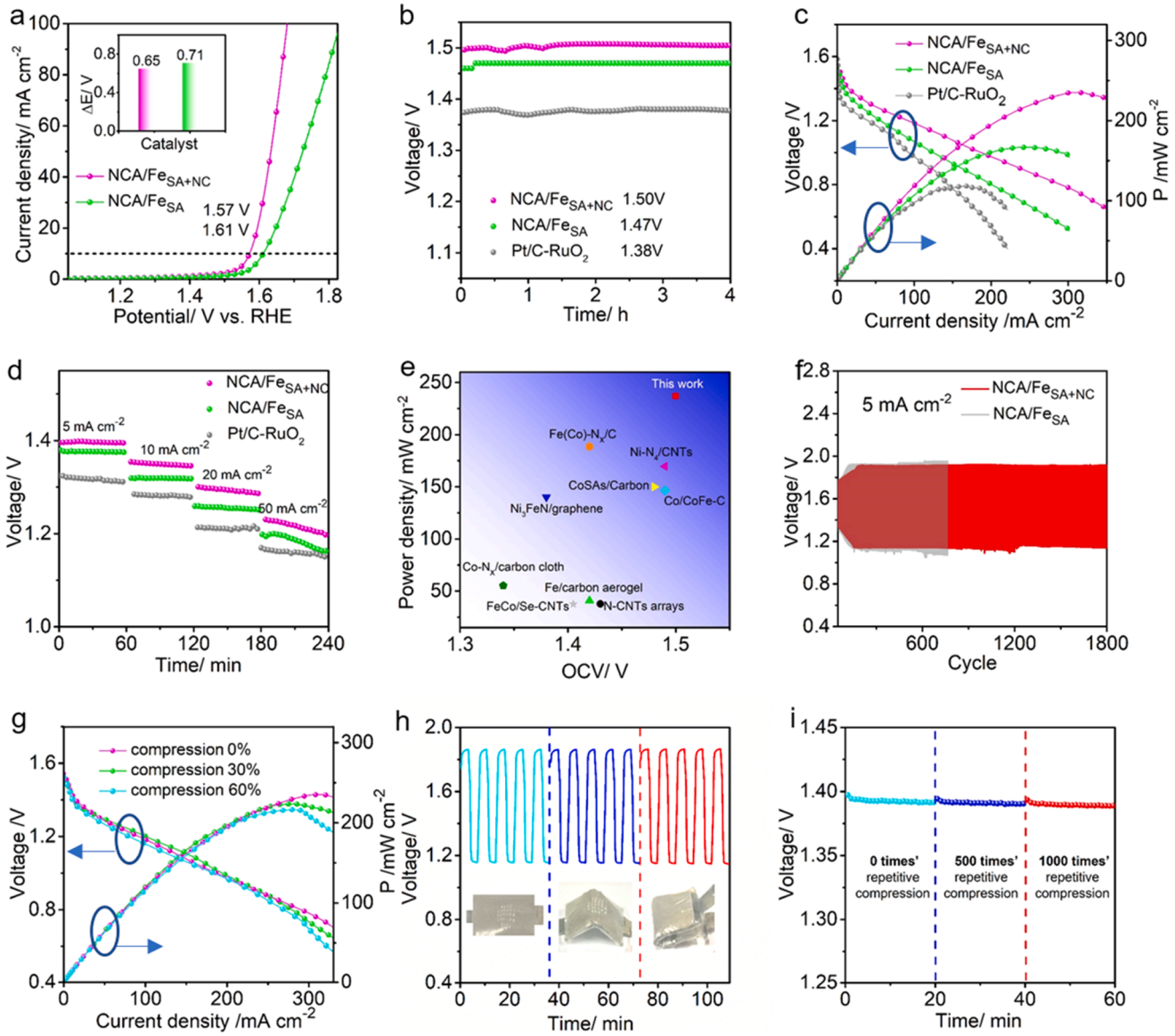

Fig. 6. (a) OER polarization curves of NCA/Fe_{SA+NC} and NCA/Fe_{SA} in 1.0 M KOH. Inset shows the ΔE of the two aerogels. (b) OCV, (c) power density and (d) constant-current discharging curves of Zn//NCA/Fe_{SA+NC}, Zn//NCA/Fe_{SA} and Zn//Pt/C-RuO_2 quasi-solid batteries. (e) Performance comparison of relevant flexible Zn-air batteries. (f) Galvanostatic charging and discharging curves at the current density of 5 mA cm^{-2} for Zn//NCA/Fe_{SA+NC} and Zn//NCA/Fe_{SA} batteries. (g) Compression, (h) repetitive bending, and (i) repetitive compression experiments of the Zn//NCA/Fe_{SA+NC} batteries.

rechargeable metal-air batteries, flexible zinc-air batteries were assembled by utilizing NCA/Fe_{SA+NC} or NCA/Fe_{SA} as the air cathode, a high-purity Zn plate as the anode and a PAA hydrogel as the flexible electrolyte. A comparative battery was also assembled by using a combination of commercial Pt/C and RuO_2 as the cathode catalysts. As manifested in Fig. 6b, the Zn//NCA/Fe_{SA+NC} battery exhibited an open circuit voltage (OCV) of 1.50 V, 30 and 120 mV higher than those of Zn//NCA/Fe_{SA} and Zn//Pt/C-RuO_2 batteries, respectively. The Zn//NCA/Fe_{SA+NC} battery also exhibited a maximum power density of 236 mW cm^{-2} (Fig. 6c), much greater than those of Zn//NCA/Fe_{SA+NC} (170 mW cm^{-2}) and Zn//Pt/C-RuO_2 batteries (119 mW cm^{-2}). In fact, the Zn//NCA/Fe_{SA+NC} battery showed a markedly higher discharge voltage with the current density varied from 5 to 50 mA cm^{-2} (Fig. 6d). Notably, this Zn//NCA/Fe_{SA+NC} battery outperformed most flexible zinc–air batteries and even the liquid ones, in terms of the OCV and maximum power density (Fig. 6e, Table S11) [59–70]. Fig. 6f shows the galvanostatic charging and discharging curves with the current density set at 5 mA cm^{-2}. The Zn//NCA/Fe_{SA} battery exhibited a voltage gap of 0.90 V and a 54.1% round-trip efficiency after merely 770 continuous charge-discharge cycles. By sharp contrast, the voltage gap was much narrower at only 0.79 V for the Zn//NCA/Fe_{SA+NC} battery, and the round-trip efficiency higher at 59.3%, even after 1800 cycles, indicating markedly enhanced activity and durability. Significantly, 95% and 92% of the maximum power density of this Zn//NCA/Fe_{SA+NC} battery was retained when the PAA layer was compressed by 30% and 60%, respectively (Fig. 6g), and the discharge-charge voltages remained almost unchanged when the battery was bended by 120° or even 180° (Fig. 6h). After 1000 repetitive compressions, the Zn//NCA/Fe_{SA+NC} battery exhibited negligible diminishment of the discharging voltage (Fig. 6i). All these indicate excellent mechanical flexibility of the Zn//NCA/Fe_{SA+NC} battery.

Notably, the carbon aerogels can even be used for low-temperature Zn-air batteries, which can find applications under special circumstances, such as polar expedition and space exploration. As the electrode reaction kinetics and ionic conductivity is significantly diminished at low temperatures, the device operation requires effective electrode

catalysts that can function under the subambient conditions. A low-temperature Zn-air battery was then constructed by following the same procedure except that a PAM hydrogel containing dimethyl sulfoxide was used instead as the electrolyte and anti-freezing agent. As depicted in Fig. 7a and 7b, the resultant Zn//NCA/Fe_{SA+NC} battery delivered a high OCV of 1.49 V and a maximum power density of 97.0 mW cm^{-2} at −20 °C, and 1.47 V and 49.0 mW cm^{-2} at −40 °C. The Zn//NCA/Fe_{SA+NC} battery also showed a stable discharge voltage when current density was varied widely from 0.2 to 5.0 mA cm^{-2}, and reached a discharge voltage of 1.36 V at −20 °C and 1.31 V at −40 °C at the current density of 1.0 mA cm^{-2} (Fig. 7c). Table S12 lists the performances of relevant low-temperature Zn-air batteries reported recently [71–77], and this Zn//NCA/Fe_{SA+NC} battery can be seen to clearly outperform most of them (Fig. 7d). Remarkably, after 2300 continuous galvanostatic charging and discharging cycles at 1.0 mA cm^{-2} at −40 °C, this Zn//NCA/Fe_{SA+NC} battery retained a stable discharging plateau with a small voltage gap of 0.32 V and a high round-trip efficiency of 81.4%, confirming excellent low-temperature adaptability and great advantage for practical application even at sub-zero temperatures (Fig. 7e). As depicted in Fig. 7f, only two Zn//NCA/Fe_{SA+NC} batteries in series were needed to power a LED pattern at −40 °C. These results corroborate the highly efficient and freeze-tolerant Zn-air battery assembled by the designed NCA/Fe_{SA+NC} catalysts.

4. Conclusion

In summary, Fe nanoclusters were formed in the proximity of Fe single atom sites embedded in N-doped carbon aerogels (NCA/Fe_{SA+NC}) via a facile two-step pyrolysis method using biomass hydrogels as the precursor and template. Spectroscopic measurements suggested electron-enrichment and reduced magnetic moment of the Fe single

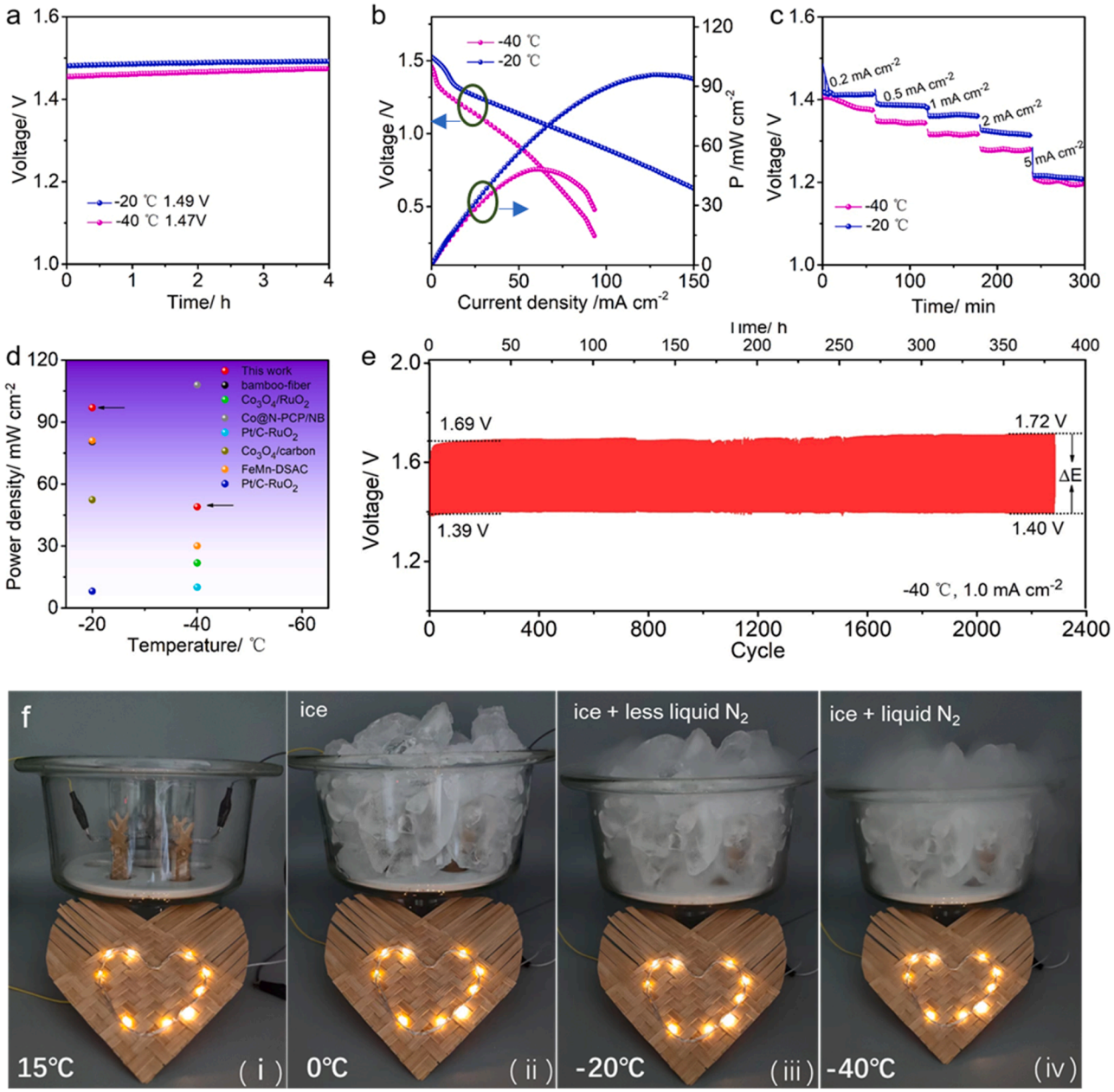

Fig. 7. (a) OCV, (b) power density and (c) constant-current discharging curves of Zn//NCA/Fe_{SA+NC} quasi-solid batteries at subambient temperatures. (d) Performance comparison of flexible Zn-air batteries at low temperatures. (e) Galvanostatic charging and discharging curves at the current density of 1.0 mA cm^{-2}. (f) Photographs of a LED pattern powered by two tandem Zn//NCA/Fe_{SA+NC} batteries at different temperatures (from 15 to —40 °C).

atoms by the adjacent Fe nanoclusters, as compared to the aerogels containing only Fe single atoms. This led to positive effects on the electrocatalytic activity and anti-oxidation stability, which was indeed attested in electrochemical measurements of the ORR and OER performances. Consistent results were obtained from first-principles calculations. With such an excellent bifunctional activity, the NCA/Fe_{SA+NC} aerogels were utilized as the oxygen cathode for flexible zinc-air batteries, which displayed a remarkable performance at ambient and even subambient temperatures (down to −40 °C), within the context of OCV, power density and durability, in comparison to those based on commercial benchmarks. Taken together, these results put forward a unique strategy in the optimization of both stability and activity of M−N−C nanocomposite catalysts for electrochemical energy conversion and storage.

CRediT authorship contribution statement

Yang Chen: Conceptualization, Investigation, Writing – original draft. **Ting He:** Conceptualization, Investigation, Writing – original draft. **Qiming Liu:** Visualization, Investigation, Resources. **Yongfeng Hu:** Visualization, Investigation, Resources. **Hao Gu:** Data curation, Software. **Liu Deng:** Data curation, Software. **Hongtao Liu:** Funding acquisition, editing. **Youcai Liu:** Funding acquisition, editing. **You-Nian Liu:** Funding acquisition, editing. **Yi Zhang:** Supervision, Funding acquisition, Writing – review & editing. **Shaowei Chen:** Supervision, Funding acquisition, Writing – review & editing. **Xiaoping Ouyang:** Supervision, Funding acquisition, Writing – review & editing.

Declaration of Competing Interest

The authors declare that they have no known competing financial interests or personal relationships that could have appeared to influence the work reported in this paper.

Data Availability

Data will be made available on request.

Acknowledgments

H. T. L. acknowledges support from the National Key R&D Program of China (No. 2019YFA0210300). Y. Z. acknowledges support from the National Natural Science Foundation of China (21972169, 21773311) and Hunan Provincial Science and Technology Plan Project (2019TP1001). T. H. thanks the Postdoctoral Research Foundation of Central South University (140050038). Y. C. is supported by the Fundamental Research Funds for the Central Universities of Central South University (1053320210820). L. D. acknowledges support from the National Natural Science Foundation of China (21878342 and 22178393), the Foundation of State Key Laboratory of Coal Conversion, Shanxi, China (J21–22-609), and the Hunan Provincial Science and Technology Plan Project, China (2020JJ3044). S. W. C. acknowledges partial support from the National Science Foundation (CHE-2003685 and CHE-1900235). The authors thank Mohsen Shakouri (Canadian Light Source) for performing the XAS tests, and Eceshi (www.eceshi.com) and high-performance computing center of CSU for the computation work.

Appendix A. Supporting information

Supplementary data associated with this article can be found in the online version at doi:10.1016/j.apcatb.2022.122163.

References

[1] Z. Liu, X. Luo, L. Qin, G. Fang, S. Liang, Progress and prospect of low-temperature zinc metal batteries, Adv. Powder Mater. 1 (2022), 100011, https://doi.org/10.1016/j.apmate.2021.10.002.
[2] C. Lai, J. Fang, X. Liu, M. Gong, T. Zhao, T. Shen, K. Wang, K. Jiang, D. Wang, In situ coupling of NiFe nanoparticles with N-doped carbon nanofibers for Zn-air batteries driven water splitting, Appl. Catal., B 285 (2021), 119856, https://doi.org/10.1016/j.apcatb.2020.119856.
[3] H.-F. Wang, C. Tang, B. Wang, B.-Q. Li, X. Cui, Q. Zhang, Defect-rich carbon fiber electrocatalysts with porous graphene skin for flexible solid-state zinc–air batteries, Energy Storage Mater. 15 (2018) 124–130, https://doi.org/10.1016/j.ensm.2018.03.022.
[4] C.X. Zhao, J.N. Liu, N. Yao, J. Wang, D. Ren, X. Chen, B.Q. Li, Q. Zhang, Can aqueous zinc–air batteries work at sub-zero temperatures? Angew. Chem. Int. Ed. 133 (2021) 15409–15413, https://doi.org/10.1002/anie.202104171.
[5] Q. Wang, Y. Lei, Z. Chen, N. Wu, Y. Wang, B. Wang, Y. Wang, Fe/Fe_3C@C nanoparticles encapsulated in N-doped graphene–CNTs framework as an efficient bifunctional oxygen electrocatalyst for robust rechargeable Zn–air batteries, J. Mater. Chem. A 6 (2018) 516–526, https://doi.org/10.1039/C7TA08423D.
[6] T. He, X. Wang, H. Wu, H. Xue, P. Xue, J. Ma, M. Tan, S. He, R. Shen, L. Yi, Y. Zhang, J. Xiang, In situ fabrication of defective CoN_x single clusters on reduced graphene oxide sheets with excellent electrocatalytic activity for oxygen reduction, ACS Appl. Mater. Interfaces 9 (2017) 22490–22501, https://doi.org/10.1021/acsami.7b04667.
[7] S.H. Yin, J. Yang, Y. Han, G. Li, L.Y. Wan, Y.H. Chen, C. Chen, X.M. Qu, Y.X. Jiang, S.G. Sun, Construction of highly active metal-containing nanoparticles and FeCo-N_4 composite sites for the acidic oxygen reduction reaction, Angew. Chem. Int. Ed. 132 (2020) 22160–22163, https://doi.org/10.1002/anie.202010013.
[8] R. Ma, G. Lin, Q. Ju, W. Tang, G. Chen, Z. Chen, Q. Liu, M. Yang, Y. Lu, J. Wang, Edge-sited Fe-N_4 atomic species improve oxygen reduction activity via boosting O_2 dissociation, Appl. Catal., B 265 (2020), 118593, https://doi.org/10.1016/j.apcatb.2020.118593.
[9] Z. Wang, J. Ang, B. Zhang, Y. Zhang, X.Y.D. Ma, T. Yan, J. Liu, B. Che, Y. Huang, X. Lu, FeCo/FeCoNi/N-doped carbon nanotubes grafted polyhedron-derived hybrid fibers as bifunctional oxygen electrocatalysts for durable rechargeable zinc–air battery, Appl. Catal., B 254 (2019) 26–36, https://doi.org/10.1016/j.apcatb.2019.04.027.
[10] Q. Xu, H. Jiang, Y. Li, D. Liang, Y. Hu, C. Li, In-situ enriching active sites on co-doped Fe-Co_4N@N-C nanosheet array as air cathode for flexible rechargeable Zn-air batteries, Appl. Catal., B 256 (2019), 117893, https://doi.org/10.1016/j.apcatb.2019.117893.
[11] Y. Lin, K. Liu, K. Chen, Y. Xu, H. Li, J. Hu, Y.-R. Lu, T.-S. Chan, X. Qiu, J. Fu, M. Liu, Tuning charge distribution of FeN_4 via external n for enhanced oxygen reduction reaction, ACS Catal. 11 (2021) 6304–6315, https://doi.org/10.1021/acscatal.0c04966.
[12] X. Cheng, Y. Wang, Y. Lu, L. Zheng, S. Sun, H. Li, G. Chen, J. Zhang, Single-atom alloy with Pt-Co dual sites as an efficient electrocatalyst for oxygen reduction reaction, Appl. Catal., B 306 (2022), 121112, https://doi.org/10.1016/j.apcatb.2022.121112.
[13] B. Lu, Q. Liu, S. Chen, Electrocatalysis of single-atom sites: impacts of atomic coordination, ACS Catal. 10 (2020) 7584–7618, https://doi.org/10.1021/acscatal.0c01950.
[14] Z. Wang, X. Jin, C. Zhu, Y. Liu, H. Tan, R. Ku, Y. Zhang, L. Zhou, Z. Liu, S.-J. Hwang, H.J. Fan, Atomically dispersed Co_2–N_6 and Fe–N_4 costructures boost oxygen reduction reaction in both alkaline and acidic media, Adv. Mater. 33 (2021) 2104718, https://doi.org/10.1002/adma.202104718.
[15] C. Tang, L. Chen, H. Li, L. Li, Y. Jiao, Y. Zheng, H. Xu, K. Davey, S.-Z. Qiao, Tailoring acidic oxygen reduction selectivity on single-atom catalysts via modification of first and second coordination spheres, J. Am. Chem. Soc. 143 (2021) 7819–7827, https://doi.org/10.1021/jacs.1c03135.
[16] C. Tang, B. Wang, H.-F. Wang, Q. Zhang, Defect engineering toward atomic Co–N_x–C in hierarchical graphene for rechargeable flexible solid Zn-Air batteries, Adv. Mater. 29 (2017) 1703185, https://doi.org/10.1002/adma.201703185.
[17] G. Chen, P. Liu, Z. Liao, F. Sun, Y. He, H. Zhong, T. Zhang, E. Zschech, M. Chen, G. Wu, J. Zhang, X. Feng, Zinc-mediated template synthesis of Fe-N-C electrocatalysts with densely accessible Fe-Nx active sites for efficient oxygen reduction, Adv. Mater. 32 (2020) 1907399, https://doi.org/10.1002/adma.201907399.
[18] J. Liu, Z. Gong, C. Allen, W. Ge, H. Gong, J. Liao, J. Liu, K. Huang, M. Yan, R. Liu, G. He, J. Dong, G. Ye, H. Fei, Edge-hosted Fe-N_3 sites on a multiscale porous carbon framework combining high intrinsic activity with efficient mass transport for oxygen reduction, Chem. Catal. 1 (2021) 1291–1307, https://doi.org/10.1016/j.checat.2021.09.012.
[19] J. Li, M.T. Sougrati, A. Zitolo, J.M. Ablett, I.C. Oğuz, T. Mineva, I. Matanovic, P. Atanassov, Y. Huang, I. Zenyuk, A. Di Cicco, K. Kumar, L. Dubau, F. Maillard, G. Dražić, F. Jaouen, Identification of durable and non-durable FeNx sites in Fe–N–C materials for proton exchange membrane fuel cells, Nat. Catal. 4 (2020) 10–19, https://doi.org/10.1038/s41929-020-00545-2.
[20] Y.-P. Ku, K. Ehelebe, A. Hutzler, M. Bierling, T. Böhm, A. Zitolo, M. Vorokhta, N. Bibent, F.D. Speck, D. Seeberger, I. Khalakhan, K.J.J. Mayrhofer, S. Thiele, F. Jaouen, S. Cherevko, Oxygen reduction reaction in alkaline media causes iron leaching from Fe–N–C electrocatalysts, J. Am. Chem. Soc. 144 (2022) 9753–9763, https://doi.org/10.1021/jacs.2c02088.
[21] W. Jiang, Y. Li, Y. Xu, T. Jiang, M. Zhao, M. Deng, R. Wu, Y. Wang, Carbon nanotube-bridged N-doped mesoporous carbon nanosphere with atomic and

nanoscaled M (M = Fe, Co) species for synergistically enhanced oxygen reduction reaction, Chem. Eng. J. 421 (2021), 129689, https://doi.org/10.1016/j.cej.2021.129689.
[22] M. Xiao, Z. Xing, Z. Jin, C. Liu, J. Ge, J. Zhu, Y. Wang, X. Zhao, Z. Chen, Preferentially engineering FeN_4 edge sites onto graphitic nanosheets for highly active and durable oxygen electrocatalysis in rechargeable Zn–Air batteries, Adv. Mater. 32 (2020) 2004900, https://doi.org/10.1002/adma.202004900.
[23] H. Li, S. Di, P. Niu, S. Wang, J. Wang, L. Li, A durable half-metallic diatomic catalyst for efficient oxygen reduction, Energy Environ. Sci. 15 (2022) 1601–1610, https://doi.org/10.1039/D1EE03194E.
[24] Y. Chen, S. Hu, F. Nichols, F. Bridges, S. Kan, T. He, Y. Zhang, S. Chen, Carbon aerogels with atomic dispersion of binary iron–cobalt sites as effective oxygen catalysts for flexible zinc–air batteries, J. Mater. Chem. A 8 (2020) 11649–11655, https://doi.org/10.1039/D0TA04633G.
[25] Y. Peng, S. Chen, Electrocatalysts based on metal@carbon core@shell nanocomposites: an overview, Green Energy Environ. 3 (2018) 335–351, https://doi.org/10.1016/j.gee.2018.07.006.
[26] J. Deng, P. Ren, D. Deng, X. Bao, Enhanced electron penetration through an ultrathin graphene layer for highly efficient catalysis of the hydrogen evolution reaction, Angew. Chem. Int. Ed. 54 (2015) 2100–2104, https://doi.org/10.1002/anie.201409524.
[27] S.-N. Zhao, J.-K. Li, R. Wang, J. Cai, S.-Q. Zang, Electronically and geometrically modified single-atom Fe sites by adjacent Fe NPs for enhanced oxygen reduction, Adv. Mater. 34 (2021) 2107291, https://doi.org/10.1002/adma.202107291.
[28] S. Peng, H. Huang, D. Yu, F. Hu, S.-C. Huang, J. Song, H.-Y. Chen, L. Li, Clusters induced electron redistribution to tune oxygen reduction activity of transition metal single-atom for metal-air batteries, Angew. Chem. Int. Ed. 61 (2021), https://doi.org/10.1002/anie.202116068.
[29] X. Wan, Q. Liu, J. Liu, S. Liu, X. Liu, L. Zheng, J. Shang, R. Yu, J. Shui, Iron atom–cluster interactions increase activity and improve durability in Fe–N–C fuel cells, Nat. Commun. 13 (2022) 2963, https://doi.org/10.1038/s41467-022-30702-z.
[30] J. Liu, T. He, Q. Wang, Z. Zhou, Y. Zhang, H. Wu, Q. Li, J. Zheng, Z. Sun, Y. Lei, J. Ma, Y. Zhang, Confining ultrasmall bimetallic alloys in porous N–carbon for use as scalable and sustainable electrocatalysts for rechargeable Zn–air batteries, J. Mater. Chem. A 7 (2019) 12451–12456, https://doi.org/10.1039/C9TA02264C.
[31] T. He, Y. Zhang, Y. Chen, Z. Zhang, H.-Y. Wang, Y. Hu, M. Liu, C.-W. Pao, J.-L. Chen, L.-Y. Chang, Z. Sun, J. Xiang, Y. Zhang, S. Chen, Single iron atoms stabilized by microporous defects of biomass-derived carbon aerogels as high-performance electrocatalysts for aluminium-air battery, J. Mater. Chem. A 7 (2019) 20840–20846, https://doi.org/10.1039/C9TA05981D.
[32] Y. Song, T. He, Y. Zhang, C. Yin, Y. Chen, Q. Liu, Y. Zhang, S. Chen, Cobalt single atom sites in carbon aerogels for ultrasensitive enzyme-free electrochemical detection of glucose, J. Electroanal. Chem. 906 (2022), 116024, https://doi.org/10.1016/j.jelechem.2022.116024.
[33] X. Ao, W. Zhang, Z. Li, J.-G. Li, L. Soule, X. Huang, W.-H. Chiang, H.M. Chen, C. Wang, M. Liu, X.C. Zeng, Markedly Enhanced Oxygen Reduction Activity of Single-Atom Fe Catalysts via Integration with Fe Nanoclusters, ACS Nano 13 (2019) 11853–11862, https://doi.org/10.1021/acsnano.9b05913.
[34] Y. Li, R. Cao, L. Li, X. Tang, T. Chu, B. Huang, K. Yuan, Y. Chen, Simultaneously integrating single atomic cobalt sites and Co_9S_8 nanoparticles into hollow carbon nanotubes as trifunctional electrocatalysts for Zn–Air batteries to drive water splitting, Small 16 (2020) 1906735, https://doi.org/10.1002/smll.201906735.
[35] T. He, H. Xue, X. Wang, S. He, Y. Lei, Y. Zhang, R. Shen, Y. Zhang, J. Xiang, Architecture of CoNx single clusters on nanocarbon as excellent oxygen reduction catalysts with high-efficient atomic utilization, Nanoscale 9 (2017) 8341–8348, https://doi.org/10.1039/C7NR02165H.
[36] Y. Li, X.F. Lu, S. Xi, D. Luan, X. Wang, X.W. Lou, Synthesis of N-doped highly graphitic carbon urchin-like hollow structures loaded with single-Ni atoms towards efficient CO_2 electroreduction, Angew. Chem. Int. Ed. 61 (2022), e202201491, https://doi.org/10.1002/anie.202201491.
[37] X. Kang, I. Di Bernardo, H. Yang, J.F. Torres, L. Zhang, Metal–organic framework microdomains in 3D conductive host as polysulfide inhibitor for fast, long-cycle Li–S batteries, Appl. Surf. Sci. 535 (2021), 147680, https://doi.org/10.1016/j.apsusc.2020.147680.
[38] T. He, Y. Song, Y. Chen, X. Song, B. Lu, Q. Liu, H. Liu, Y. Zhang, X. Ouyang, S. Chen, Atomically dispersed ruthenium in carbon aerogels as effective catalysts for pH-universal hydrogen evolution reaction, Chem. Eng. J. 442 (2022), 136337, https://doi.org/10.1016/j.cej.2022.136337.
[39] Y. Chen, T. He, D. Liao, Q. Li, Y. Song, H. Xue, Y. Zhang, Carbon aerogels with nickel@N-doped carbon core-shell nanoclusters as electrochemical sensors for simultaneous determination of hydroquinone and catechol, Electrochim. Acta 414 (2022), 140199, https://doi.org/10.1016/j.electacta.2022.140199.
[40] T. He, Y. Peng, Q. Li, J.E. Lu, Q. Liu, R. Mercado, Y. Chen, F. Nichols, Y. Zhang, S. Chen, Nanocomposites based on ruthenium nanoparticles supported on cobalt and nitrogen-codoped graphene nanosheets as bifunctional catalysts for electrochemical water splitting, ACS Appl. Mater. Interfaces 11 (2019) 46912–46919, https://doi.org/10.1021/acsami.9b17056.
[41] W. Zhai, S. Huang, C. Lu, X. Tang, L. Li, B. Huang, T. Hu, K. Yuan, X. Zhuang, Y. Chen, Simultaneously integrate iron single atom and nanocluster triggered tandem effect for boosting oxygen electroreduction, Small 18 (2022) 2107225, https://doi.org/10.1002/smll.202107225.
[42] T. Mineva, I. Matanovic, P. Atanassov, M.-T. Sougrati, L. Stievano, M. Clémancey, A. Kochem, J.-M. Latour, F. Jaouen, Understanding active sites in pyrolyzed Fe–N–C catalysts for fuel cell cathodes by bridging density functional theory calculations and 57Fe Mössbauer spectroscopy, ACS Catal. 9 (2019) 9359–9371, https://doi.org/10.1021/acscatal.9b02586.
[43] U.I. Koslowski, I. Abs-Wurmbach, S. Fiechter, P. Bogdanoff, Nature of the catalytic centers of porphyrin-based electrocatalysts for the ORR: a correlation of kinetic current density with the site density of Fe−N_4 centers, J. Phys. Chem. C. 112 (2008) 15356–15366, https://doi.org/10.1021/jp802456e.
[44] Z. Li, Z. Zhuang, F. Lv, H. Zhu, L. Zhou, M. Luo, J. Zhu, Z. Lang, S. Feng, W. Chen, L. Mai, S. Guo, The marriage of the FeN_4 moiety and mxene boosts oxygen reduction catalysis: Fe 3d electron delocalization matters, Adv. Mater. 30 (2018) 1803220, https://doi.org/10.1002/adma.201803220.
[45] T. He, B. Lu, Y. Chen, Y. Wang, Y. Zhang, J.L. Davenport, A.P. Chen, C.-W. Pao, M. Liu, Z. Sun, Nanowrinkled carbon aerogels embedded with FeNx Sites as effective oxygen electrodes for rechargeable zinc-air battery, Research 2019 (2019) 6813585, https://doi.org/10.34133/2019/6813585.
[46] M. Chen, X. Li, F. Yang, B. Li, T. Stracensky, S. Karakalos, S. Mukerjee, Q. Jia, D. Su, G. Wang, G. Wu, H. Xu, Atomically dispersed MnN_4 catalysts via environmentally benign aqueous synthesis for oxygen reduction: mechanistic understanding of activity and stability improvements, ACS Catal. 10 (2020) 10523–10534, https://doi.org/10.1021/acscatal.0c02490.
[47] J. Miao, Y. Zhu, J. Lang, J. Zhang, S. Cheng, B. Zhou, L. Zhang, P.J.J. Alvarez, M. Long, Spin-state-dependent peroxymonosulfate activation of single-atom M–N moieties via a radical-free pathway, ACS Catal. 11 (2021) 9569–9577, https://doi.org/10.1021/acscatal.1c02031.
[48] Z. Sun, L. Lin, J. He, D. Ding, T. Wang, J. Li, M. Li, Y. Liu, Y. Li, M. Yuan, B. Huang, H. Li, G. Sun, Regulating the spin state of feiii enhances the magnetic effect of the molecular catalysis mechanism, J. Am. Chem. Soc. 144 (2022) 8204–8213, https://doi.org/10.1021/jacs.2c01153.
[49] L. Peng, L. Shang, T. Zhang, G.I.N. Waterhouse, Recent advances in the development of single-atom catalysts for oxygen electrocatalysis and zinc–air batteries, Adv. Energy Mater. 10 (2020) 2003018, https://doi.org/10.1002/aenm.202003018.
[50] X. Cui, L. Gao, S. Lei, S. Liang, J. Zhang, C.D. Sewell, W. Xue, Q. Liu, Z. Lin, Y. Yang, Simultaneously crafting single-atomic Fe sites and graphitic layer-wrapped Fe_3C nanoparticles encapsulated within mesoporous carbon tubes for oxygen reduction, Adv. Funct. Mater. 31 (2021) 2009197, https://doi.org/10.1002/adfm.202009197.
[51] H. Fei, J. Dong, Y. Feng, C.S. Allen, C. Wan, B. Volosskiy, M. Li, Z. Zhao, Y. Wang, H. Sun, P. An, W. Chen, Z. Guo, C. Lee, D. Chen, I. Shakir, M. Liu, T. Hu, Y. Li, A. I. Kirkland, X. Duan, Y. Huang, General synthesis and definitive structural identification of MN_4C_4 single-atom catalysts with tunable electrocatalytic activities, Nat. Catal. 1 (2018) 63–72, https://doi.org/10.1038/s41929-017-0008-y.
[52] J. Ji, L. Wu, S. Zhou, T. Qiu, Z. Li, L. Wang, L. Zhang, L. Ma, M. Ling, S. Zhou, C. Liang, Regulating electronic structure of single-atom catalysts toward efficient bifunctional oxygen electrocatalysis, Small Method 6 (2022) 2101511, https://doi.org/10.1002/smtd.202101511.
[53] H. Yang, S. Gao, D. Rao, X. Yan, Designing superior bifunctional electrocatalyst with high-purity pyrrole-type CoN_4 and adjacent metallic cobalt sites for rechargeable Zn-air batteries, Energy Storage Mater. 46 (2022) 553–562, https://doi.org/10.1016/j.ensm.2022.01.040.
[54] W.W. Xie, T.Z. Tian, M. Yang, N.W. Li, L. Yu, Formation of hollow frameworks of dual-sided Fe/Fe_3C@N-doped carbon nanotubes as bifunctional oxygen electrocatalyst for Zn-air batteries, Appl. Catal., B 317 (2022), 121760, https://doi.org/10.1016/j.apcatb.2022.121760.
[55] Y. Tan, Z. Zhang, Z. Lei, L. Yu, W. Wu, Z. Wang, N. Cheng, Electronic modulation optimizes OH* intermediate adsorption on Co-Nx-C sites via coupling CoNi alloy in hollow carbon nanopolyhedron toward efficient reversible oxygen electrocatalysis, Appl. Catal., B 304 (2022), 121006, https://doi.org/10.1016/j.apcatb.2021.121006.
[56] Y.-j Wu, X.-h Wu, T.-x Tu, P.-f Zhang, J.-t Li, Y. Zhou, L. Huang, S.-g Sun, Controlled synthesis of FeNx-CoNx dual active sites interfaced with metallic Co nanoparticles as bifunctional oxygen electrocatalysts for rechargeable Zn-air batteries, Appl. Catal., B 278 (2020), 119259, https://doi.org/10.1016/j.apcatb.2020.119259.
[57] J.-C. Li, Y. Meng, L. Zhang, G. Li, Z. Shi, P.-X. Hou, C. Liu, H.-M. Cheng, M. Shao, Dual-phasic carbon with Co single atoms and nanoparticles as a bifunctional oxygen electrocatalyst for rechargeable Zn–Air batteries, Adv. Funct. Mater. 31 (2021) 2103360, https://doi.org/10.1002/adfm.202103360.
[58] Z. Yu, C. Si, A.P. LaGrow, Z. Tai, W.A. Caliebe, A. Tayal, M.J. Sampaio, J.P. S. Sousa, I. Amorim, A. Araujo, L. Meng, J.L. Faria, J. Xu, B. Li, L. Liu, Iridium–iron diatomic active sites for efficient bifunctional oxygen electrocatalysis, ACS Catal. 12 (2022) 9397–9409, https://doi.org/10.1021/acscatal.2c01861.
[59] K.N. Dinh, Z. Pei, Z. Yuan, V.C. Hoang, L. Wei, Q. Huang, X. Liao, C. Liu, Y. Chen, Q. Yan, The on-demand engineering of metal-doped porous carbon nanofibers as efficient bifunctional oxygen catalysts for high-performance flexible Zn–air batteries, J. Mater. Chem. A 8 (2020) 7297–7308, https://doi.org/10.1039/C9TA13651G.
[60] C. Lai, M. Gong, Y. Zhou, J. Fang, L. Huang, Z. Deng, X. Liu, T. Zhao, R. Lin, K. Wang, K. Jiang, H. Xin, D. Wang, Sulphur modulated Ni_3FeN supported on N/S co-doped graphene boosts rechargeable/flexible Zn-air battery performance, Appl. Catal. B 274 (2020), 119086, https://doi.org/10.1016/j.apcatb.2020.119086.
[61] Z. Li, J. Yang, X. Ge, Y.-P. Deng, G. Jiang, H. Li, G. Sun, W. Liu, Y. Zheng, H. Dou, H. Jiao, J. Zhu, N. Li, Y. Hu, M. Feng, Z. Chen, Self-assembly of colloidal MOFs derived yolk-shelled microcages as flexible air cathode for rechargeable Zn-air batteries, Nano Energy 89 (2021), 106314, https://doi.org/10.1016/j.nanoen.2021.106314.

[62] L. Liu, X. Zhang, F. Yan, B. Geng, C. Zhu, Y. Chen, Self-supported N-doped CNT arrays for flexible Zn–air batteries, J. Mater. Chem. A 8 (2020) 18162–18172, https://doi.org/10.1039/D0TA05510G.
[63] Y. Niu, X. Teng, S. Gong, M. Xu, S.-G. Sun, Z. Chen, Engineering two-phase bifunctional oxygen electrocatalysts with tunable and synergetic components for flexible Zn–Air batteries, Nano-Micro Lett. 13 (2021) 126, https://doi.org/10.1007/s40820-021-00650-2.
[64] F. Wang, G. Li, X. Meng, S. Xu, W. Ma, One-dimensional $Mn_3O_4/NiCo_2S_4$ nanocomposites as high-performance bifunctional electrocatalyst for rechargeable liquid/flexible Zn-air batteries, J. Power Sources 462 (2020), 228162, https://doi.org/10.1016/j.jpowsour.2020.228162.
[65] K. Wu, L. Zhang, Y. Yuan, L. Zhong, Z. Chen, X. Chi, H. Lu, Z. Chen, R. Zou, T. Li, C. Jiang, Y. Chen, X. Peng, J. Lu, An iron-decorated carbon aerogel for rechargeable flow and flexible Zn–air batteries, Adv. Mater. 32 (2020) 2002292, https://doi.org/10.1002/adma.202002292.
[66] G. Zhang, H. Ge, L. Zhao, J. Liu, S. Fan, F. Wang, G. Li, Cubic $KNiFe(CN)_6$/C loaded on nickel foam for rechargeable liquid/flexible Zn-air batteries, Electrochim. Acta 397 (2021), 139278, https://doi.org/10.1016/j.electacta.2021.139278.
[67] H. Zhang, M. Zhao, H. Liu, S. Shi, Z. Wang, B. Zhang, L. Song, J. Shang, Y. Yang, C. Ma, L. Zheng, Y. Han, W. Huang, Ultrastable FeCo bifunctional electrocatalyst on Se-doped CNTs for liquid and flexible all-solid-state rechargeable Zn–Air batteries, Nano Lett. 21 (2021) 2255–2264, https://doi.org/10.1021/acs.nanolett.1c00077.
[68] Z. Zhang, X. Zhao, S. Xi, L. Zhang, Z. Chen, Z. Zeng, M. Huang, H. Yang, B. Liu, S. J. Pennycook, P. Chen, Atomically dispersed cobalt trifunctional electrocatalysts with tailored coordination environment for flexible rechargeable Zn–Air battery and self-driven water splitting, Adv. Energy Mater. 10 (2020) 2002896, https://doi.org/10.1002/aenm.202002896.
[69] M. Zhao, H. Liu, H. Zhang, W. Chen, H. Sun, Z. Wang, B. Zhang, L. Song, Y. Yang, C. Ma, Y. Han, W. Huang, A pH-universal ORR catalyst with single-atom iron sites derived from a double-layer MOF for superior flexible quasi-solid-state rechargeable Zn–air batteries, Energy Environ. Sci. 14 (2021) 6455–6463, https://doi.org/10.1039/D1EE01602D.
[70] Y. Zhou, M. Xie, Y. Song, D. Yan, Z. Wang, S. Zhang, C. Deng, Edge-enriched Ni-N_4 atomic sites embedded enoki-mushroom-like carbon nanotubes assembling hollow fibers for CO_2 conversion and flexible Zn-air battery, Energy Storage Mater. 47 (2022) 235–248, https://doi.org/10.1016/j.ensm.2022.02.021.
[71] N. Sun, F. Lu, Y. Yu, L. Su, X. Gao, L. Zheng, Alkaline double-network hydrogels with high conductivities, superior mechanical performances, and antifreezing properties for solid-state zinc–air batteries, ACS Appl. Mater. Interfaces 12 (2020) 11778–11788, https://doi.org/10.1021/acsami.0c00325.
[72] T. Cui, Y.-P. Wang, T. Ye, J. Wu, Z. Chen, J. Li, Y. Lei, D. Wang, Y. Li, Engineering dual single-atom sites on 2D ultrathin N-doped carbon nanosheets attaining ultra-low-temperature zinc-air battery, Angew. Chem. Int. Ed. 61 (2022), e202115219, https://doi.org/10.1002/anie.202115219.
[73] R. Chen, X. Xu, S. Peng, J. Chen, D. Yu, C. Xiao, Y. Li, Y. Chen, X. Hu, M. Liu, H. Yang, I. Wyman, X. Wu, A flexible and safe aqueous zinc–air battery with a wide operating temperature range from −20 to 70 °C, ACS Sustain. Chem. Eng. 8 (2020) 11501–11511, https://doi.org/10.1021/acssuschemeng.0c01111.
[74] Z. Pei, Z. Yuan, C. Wang, S. Zhao, J. Fei, L. Wei, J. Chen, C. Wang, R. Qi, Z. Liu, Y. Chen, A flexible rechargeable zinc–air battery with excellent low-temperature adaptability, Angew. Chem. Int. Ed. 59 (2020) 4793–4799, https://doi.org/10.1002/anie.201915836.
[75] D. Jiang, H. Wang, S. Wu, X. Sun, J. Li, Flexible zinc–air battery with high energy efficiency and freezing tolerance enabled by DMSO-based organohydrogel electrolyte, Small Methods 6 (2022) 2101043, https://doi.org/10.1002/smtd.202101043.
[76] Y. Zhang, H. Qin, M. Alfred, H. Ke, Y. Cai, Q. Wang, F. Huang, B. Liu, P. Lv, Q. Wei, Reaction modifier system enable double-network hydrogel electrolyte for flexible zinc-air batteries with tolerance to extreme cold conditions, Energy Storage Mater. 42 (2021) 88–96, https://doi.org/10.1016/j.ensm.2021.07.026.
[77] C. Gu, X.-Q. Xie, Y. Liang, J. Li, H. Wang, K. Wang, J. Liu, M. Wang, Y. Zhang, M. Li, H. Kong, C.-S. Liu, Small molecule-based supramolecular-polymer double-network hydrogel electrolytes for ultra-stretchable and waterproof Zn–air batteries working from −50 to 100 °C, Energy Environ. Sci. 14 (2021) 4451–4462, https://doi.org/10.1039/D1EE01134K.